Applied Catalysis B: Environmental 198 (2016) 224–233

Contents lists available at ScienceDirect

Applied Catalysis B: Environmental

journal homepage: www.elsevier.com/locate/apcatb

$Ni(OH)_2$ decorated rutile TiO_2 for efficient removal of tetracycline from wastewater

Sookwan Leong [a], Dan Li [b], Karen Hapgood [a], Xiwang Zhang [a], Huanting Wang [a,*]

[a] Department of Chemical Engineering, Monash University, Clayton, Australia
[b] Chemical and Metallurgical Engineering & Chemistry, School of Engineering and Information Technology, Murdoch University, Murdoch, Australia

ARTICLE INFO

Article history:
Received 14 February 2016
Received in revised form 15 May 2016
Accepted 20 May 2016
Available online 20 May 2016

Keywords:
Rutile
Photocatalysis
Tetracycline
Adsorption
Photodegradation

ABSTRACT

Flower-like and coral-like particles composed of rutile TiO_2 nanorods were synthesized *via* hydrolysis of $TiCl_4$ in water at room temperature and hydrothermal crystallization. The subsequent deposition of $Ni(OH)_2$ clusters resulted in enhanced adsorption property and photocatalytic activity. In particular, $Ni(OH)_2$-modified coral-like rutile TiO_2 was shown to efficiently remove 76% of tetracycline from 100 mg L^{-1} solution after 30 min adsorption and subsequent 2 h photodegradation under visible light; whereas only 57% tetracycline removal was achieved by the commercial TiO_2 (P25). In addition, the micro-sized $Ni(OH)_2$-modified rutile TiO_2 particles could be easily recovered from water after the photocatalytic process, and showed significant advantages over nano-sized photocatalysts. Our study provides a simple and green route to synthesizing photocatalysts with enhanced adsorption and photocatalytic performance for potential applications in practical water purification and wastewater treatment.

1. Introduction

Antibiotics have been widely selected in prophylaxis and therapy of human and animal diseases and as promoters for animal growth. Tetracycline, as one among the cheapest classes of antibiotics [1] has been used to treat many kinds of bacterial infections, for instance urinary tract infections, acne and gonorrhea. Additionally, tetracycline is commonly adopted in agricultural industry to prevent livestock diseases. However, like many other antibiotics, tetracycline can only be partially metabolized by humans and animals, causing the residue to be released into wastewater [1]. Because of the absence of biodegradability, the removal of tetracycline during biological process in conventional wastewater treatment plants is mainly achieved by biosorption instead of biodegradation [2,3]. This always leads to a difficulty in completely and efficiently eliminating tetracycline before effluent is discharged and it inevitably reaches natural water bodies; it has accelerated growth of antibiotic-resistant bacteria and genes in environment [4]. Among various other technologies investigated so far, photocatalytic oxidation reaction appears to be a cost- effective, high-performance and environmentally sustainable alternative to treat tetracycline wastewater.

Titanium dioxide (TiO_2) is a promising semiconductor, which has attracted great interest in a variety of applications, including water splitting and pollutant degradation [5–8]. The photocatalytic activity of TiO_2 has been shown to strongly rely on its phase structure, crystallite size, morphological characteristic, surface area and pore structure. In general, rutile TiO_2 is less often investigated as compared to its anatase phase due to its lower photocatalytic activity arising from higher positive conduction band edge potential and faster recombination rate of photoelectron and holes [9,10]. Nevertheless, in addition to higher light scattering efficiency, better chemical stability and lower production cost, rutile TiO_2 has a smaller bandgap energy of only 3.00 eV than anatase TiO_2 (3.20 eV); thus it is fundamentally interesting for developing visible light driven photocatalytic applications [11].

It is well known that the high-performance photocatalysts should possess several features, including high crystallinity and large surface area/porosity. The traditional synthetic methods utilized the phase transformation of either amorphous titania or anatase *via* high temperature calcination (e.g. 600 °C) to produce rutile TiO_2 [12,13]. However, this might unavoidably lead to agglomeration and growth of nanocrystalline particles, thus forming large particle sizes and small surface areas. Furthermore, the rutile phase prepared at low temperature exhibited better photocatalytic activity as compared with that produced at high temperature [14]. A number of prior studies reported the preparation of rutile TiO_2 at relatively low temperature; but it

* Corresponding author.
E-mail address: huanting.wang@monash.edu (H. Wang).

http://dx.doi.org/10.1016/j.apcatb.2016.05.043
0926-3373/

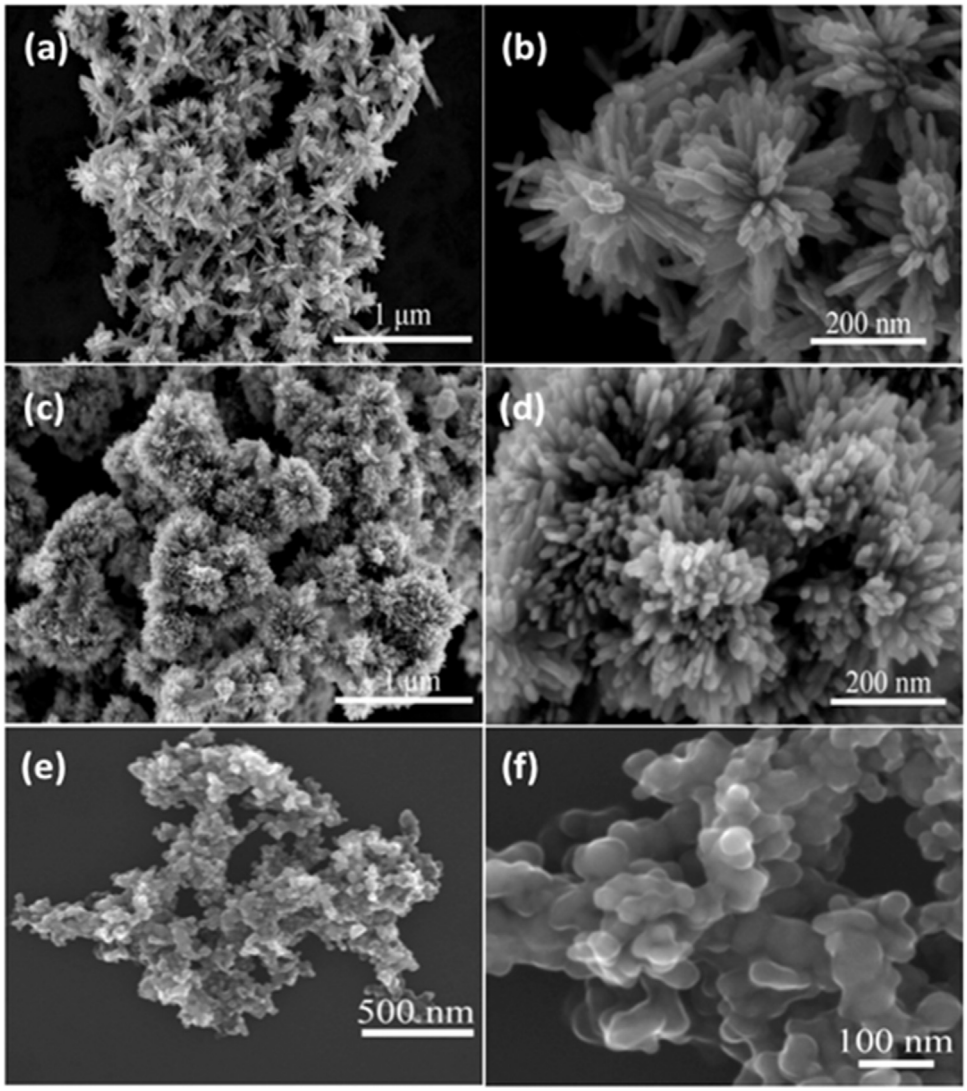

Fig. 1. SEM images of T1 (a and b), T2 (c and d) and P25 (e and f) at low and high magnification. The SEM images of P25 are taken at magnifications different from T1 and T2 for clarity.

usually required introduction of acids, solvents or other chemicals, and in turn increased synthesis complexity and cost [15,16]. On the other side, in spite of advantageously large external surfaces, small sizes of nanoparticles make them very difficult to be separated from solution after photocatalytic reaction. From a practical application perspective, forming mesocrystals, as a class of micro/nanostructured materials, which are composed of nanocrystals arranged in a regular fashion, could be an alternative solution. Three-dimensional hierarchical structure of mesocrystals offers favorable surface area and light scattering for efficient photon harvesting compared to nanocrystallites [17].

To further enhance photocatalytic activity of TiO_2, several strategies have been investigated so far, including doping with metals [18,19] and non-metals [20–22] to narrow its bandgap energy. Some composites consisting of two oxide or hydroxide particles with different energy levels have been reported with better photocatalytic activities because of more efficient charge separation [23]. For instance, the $Ni(OH)_2$/ZnO composite could potentially inhibit rapid recombination of photogenerated electrons and holes, thus enhancing photocatalytic oxidation of organic azo dyes as compared with either pure ZnO or $Ni(OH)_2$ [23]. Some previous investigations have also indicated transition-metal hydroxide $Ni(OH)_2$ is an economical and good co-catalyst when modifying TiO_2 for producing H_2 from water splitting [24,25]. Up to date, there has been no study published on applying $Ni(OH)_2$ on TiO_2 as a photocatalyst to degrade antibiotics from water under visible light illumination.

In this paper we report a simple and environmentally friendly method for synthesizing rutile TiO_2 mesocrystals, *via* hydrolysis of $TiCl_4$ in water in the absence of other chemicals at room temperature and subsequent crystallization at 180 °C. We have further modified the TiO_2 mesocrystals with $Ni(OH)_2$ clusters *via* precipitation. Their structural properties as well as adsorption and photodegradation of tetracycline were examined in detail, in comparison with the commercial TiO_2 product, P25.

2. Experimental

2.1. Chemicals

Titanium chloride ($TiCl_4$, ≥99.0%), nickel chloride ($NiCl_2$, 98%) and tetracycline (≥98.1%) were purchased from Sigma-Aldrich, Australia. Sodium hydroxide (NaOH, 32%) and Aeroxide® TiO_2 P25 were obtained from Merck, Germany and Evonik Industries, Germany, respectively. All chemicals were used as received with-

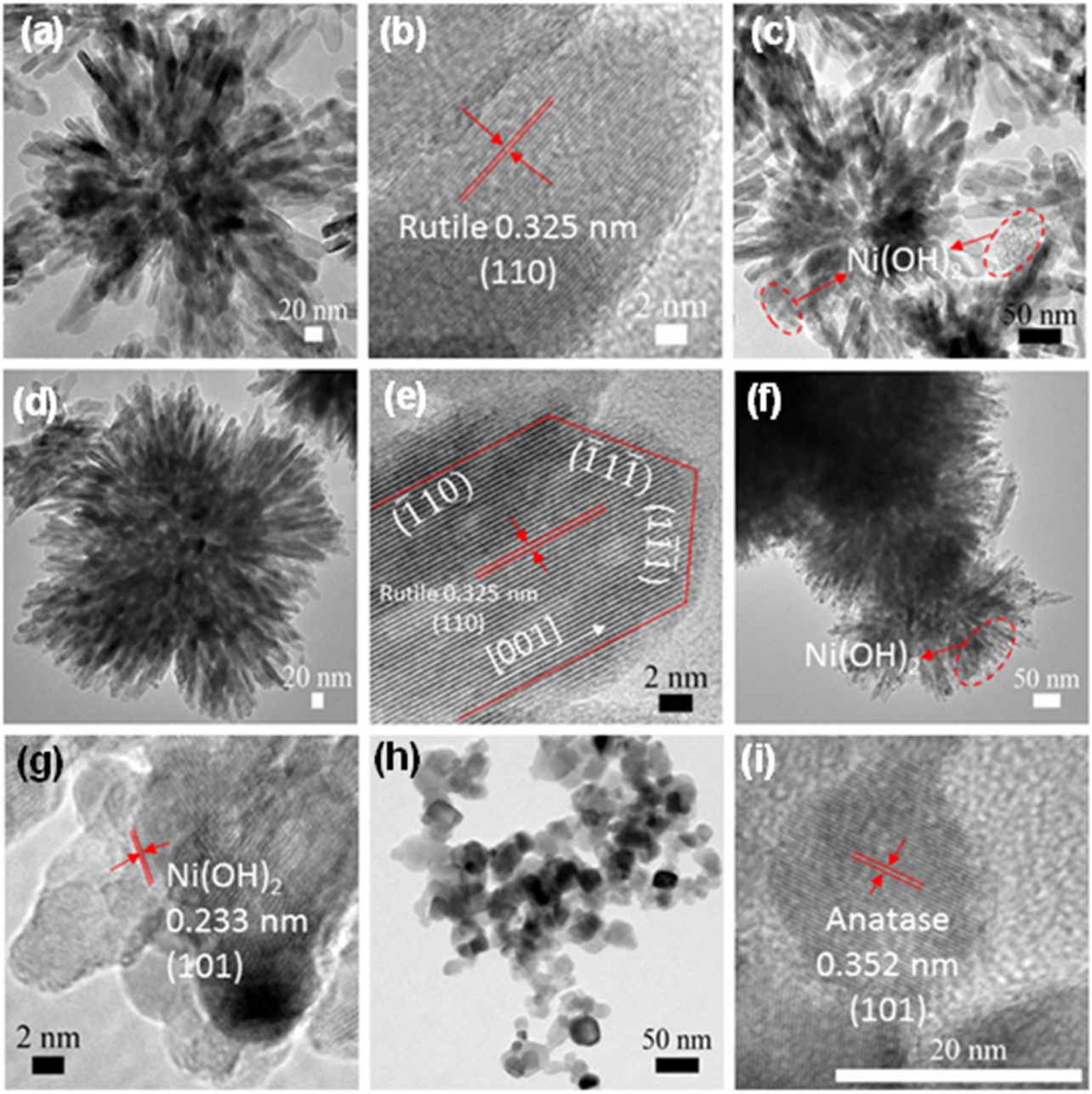

Fig. 2. TEM images of T1 (a and b), T1-Ni (c), T2 (d and e), T2-Ni (f), and P25 (g and h) at low and high magnifications. The circled material in (c) and (f) is $Ni(OH)_2$. (For interpretation of the references to colour in the text, the reader is referred to the web version of this article.)

out further treatment. Double deionized (DI) water was used for all experiments.

2.2. Preparation of TiO_2 and $Ni(OH)_2$-TiO_2 catalysts

Typically, TiO_2 mesocrystals were prepared by hydrolyzing 20 mL of 0.1 M $TiCl_4$ aqueous solution at 25 °C for 24 h and subsequently at room temperature for another 48 h. Afterwards, the white precipitate was washed with DI water and ethanol in turn for 3 times, and recovered by centrifugation. The obtained white precipitate was dried at 80 °C for 24 h, followed by crystallization at 180 °C for 6 h. The resulting TiO_2 sample was denoted as T1. The similar approach was adopted to produce the T2 sample, except for using 0.2 M $TiCl_4$ aqueous solution.

0.08 g of the as-prepared T1 or T2 was dispersed in 20 mL of 0.1 M NaOH solution and followed by adding 0.026 g of $NiCl_2$ to form $Ni(OH)_2$ precipitate (Eq. (1)). After keeping the obtained mixture stirring for 24 h, the greenish powders were separated by centrifugation; and then washed with DI water and ethanol in turn for 3 times. The resulting $Ni(OH)_2$-deposited T1 or T2 powders were dried at 80 °C for 24 h, which were denoted as T1-Ni or T2-Ni, respectively.

$$NiCl_2(s) + 2NaOH(aq) \rightarrow Ni(OH)_2(s) + 2NaCl(aq) \quad (1)$$

2.3. Characterization

Morphologies of the samples were examined using a scanning electron microscope (SEM, FEI Magellan 400 FEG, USA) and a transmission electron microscope (TEM, FEI Tecnai G2 T20 TWIN LaB6, USA). Crystal structures of the samples were investigated using an X-ray diffractometer (XRD, Miniflex 600, Rigaku, Japan) with Cu

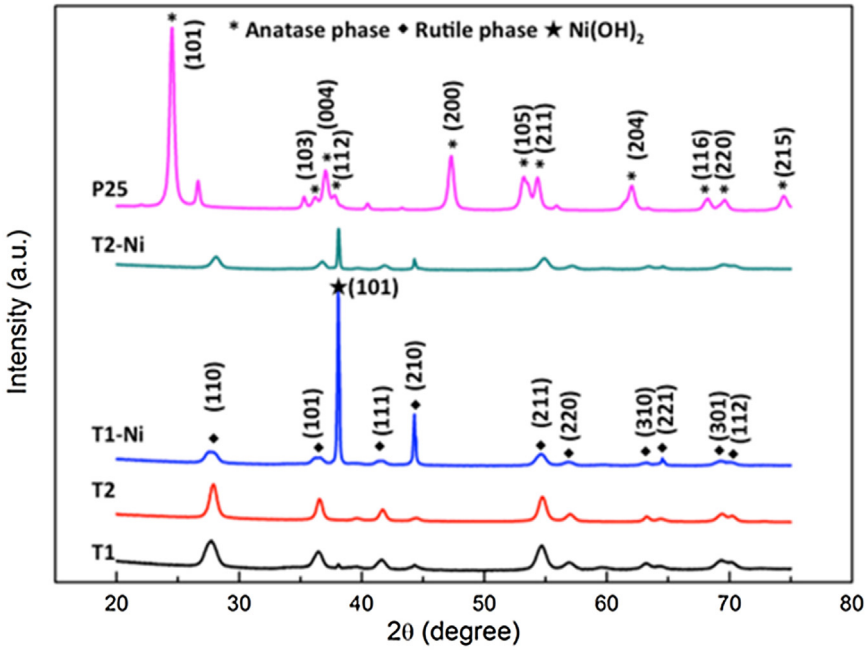

Fig. 3. XRD patterns of T1, T2, T1-Ni and T2-Ni in comparison with P25.

Kα radiation at 40 kV and 20 mA at a scan speed of 2° min^{-1} in the range of 20–75°. Nitrogen adsorption-desorption isotherms were measured at 77 K using an accelerated surface area and porosimetry system (ASAP 2020, Micromeritics, USA). Bandgap energy values were calculated using bandwidth spectra recorded by a UV–vis spectrophotometer (UV-2600, Shimadzu, Japan).

2.4. Adsorption and photocatalytic degradation test

Adsorption and photocatalytic activity properties of the samples, including T1, T2, T1-Ni, and T2-Ni, were investigated by adding 200 mg catalyst into 20 mL of 100 mg L^{-1} tetracycline solution in a water-cooling jacket vessel. Aeroxide® TiO_2 P25, denoted as P25, was also tested under the same condition as a reference. Visible light was obtained from a 200 W mercury xenon lamp (Newport Corporation, USA) with a UV-cutoff filter removing the light of wavelength less than 420 nm. The tetracycline concentration was determined by measuring the intensity of characteristic absorbance peak at 356 nm using a UV–vis spectrophotometer (UVmini-1240, Shimadzu, Japan). Prior to light irradiation, the suspension was firstly stirred in the dark for 30 min to achieve adsorption equilibrium of tetracycline on the catalyst. Subsequently, the suspension was exposed to visible light under continuous stirring for 2 h; from which 1.5 mL of the sample was taken at every 15 min.

Langmuir-Hinshelwood (L-H) model, which was simplified to the pseudo-first-order equation and shown in Eq. (2), was used to describe the heterogeneous photodegradation kinetic behavior.

$$\ln\frac{C}{C_0} = -kt \tag{2}$$

where C (mg L^{-1}) was the tetracycline concentration at a given period of time t during photodegradation, C_0 (mg L^{-1}) was the tetracycline concentration at the adsorption equilibrium, t (min) is the degradation time, and k (min^{-1}) is the reaction rate constant.

3. Results and discussion

Fig. 1 shows the low magnification and high magnification SEM images of the samples T1 (a and b), T2 (c and d) and P25 (e and f). As shown in Fig. 1e and f, the commercial TiO_2 P25 consisted of irregular particles with sizes ranging from 20 nm to 30 nm. The sample T1, synthesized from the hydrolysis of 0.1 M $TiCl_4$ and subsequent crystallization, exhibits characteristic nanorod-aggregated flower-like bundles (Fig. 1a and b). As the concentration of $TiCl_4$ in the synthetic solution was increased to 0.2 M, the resulting T2 sample shows coral-like loops consisting of nanorod aggregates (Fig. 1c and d). In both T1 and T2, those nanorods are radially arranged from the center of lumps (Fig. 1b and d). The nanorods in T2 present a smaller average size but in a greater density than those in T1, resulting in TiO_2 mesocrystals with a feature of smaller average pore size, which was later evidenced in the nitrogen adsorption-desorption results (Table 1 and Fig. 5). Previous studies suggested that nanorod nanostructures possess higher photocatalytic activity as compared with nanoparticles, because they have advantages of improving visible light scattering and absorption property, increasing reactive sites, optimizing crystal plan effect, as well as lowering recombination rate of photogenerated electrons and holes [26–28].

Table 1
BET surface area, pore volume and average pore size of T1, T2, T1-Ni, T2-Ni and P25.

Sample	BET surface area (m^2g^{-1})	Pore volume (cm^3g^{-1})	Average pore size (nm)
T1	70.2	0.37	16.9
T2	70.3	0.19	8.7
T1-Ni	91.6	0.49	17.3
T2-Ni	77.3	0.24	9.9
P25	56.3	0.29	24.7

The samples were further examined by TEM and the images are shown in Fig. 2. Similar to the morphologies shown in Fig. 1e and f, the commercial TiO_2, P25, powder is composed of nanoparticles with an average size of approximately 30 nm (Fig. 2h). The high resolution TEM (HRTEM) image (Fig. 2i) demonstrates the lattice fringes of P25 with a distance of 3.52 Å corresponding to the (101) plane of anatase TiO_2, which is in agreement with its XRD pattern shown in Fig. 3. The low magnification TEM images of T1 and T2 (Fig. 2a and d) clearly show the nanorods are agglomerated to form bundles; the sizes are consistent with those shown in the SEM images (Fig. 1b and d). The HRTEM images (Fig. 2b and e) show the lattice fringes with a distance of 3.25 Å, corresponding to the

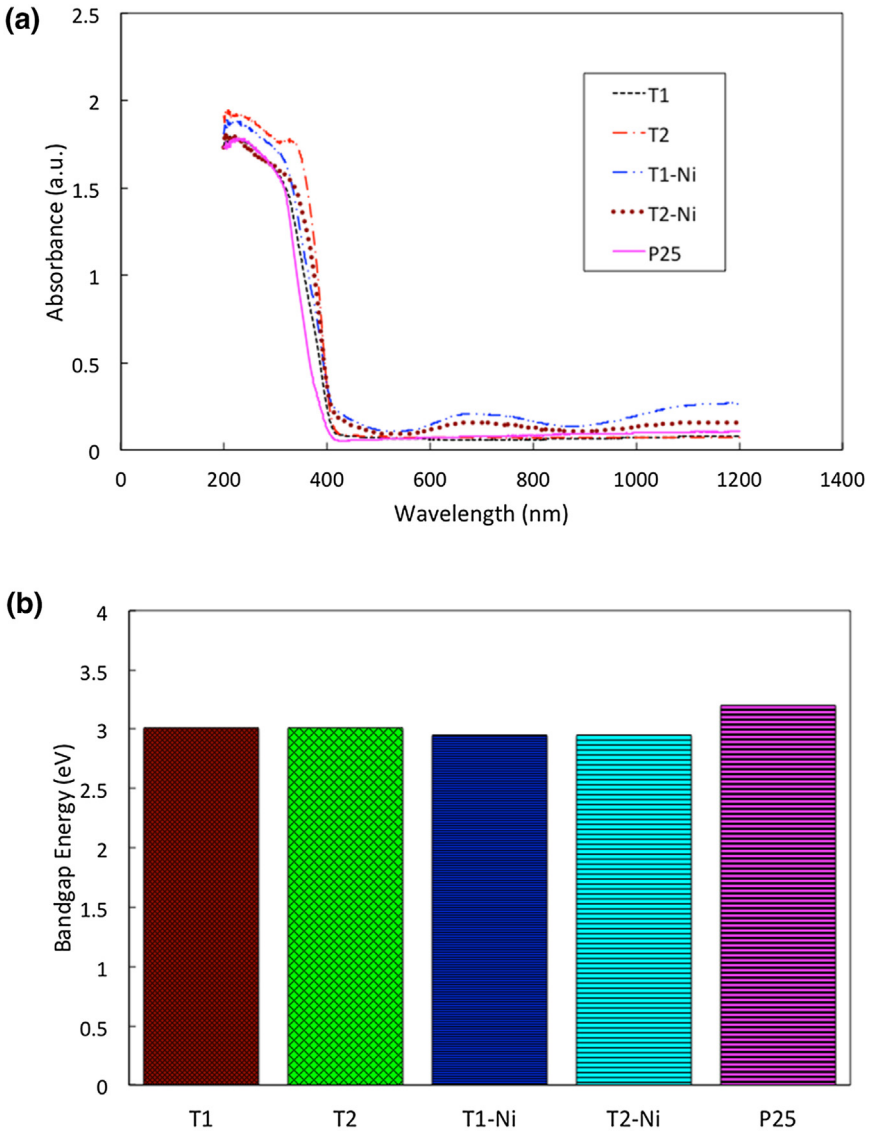

Fig. 4. (a) UV–vis diffuse-reflectance spectra and (b) bandgap.

(110) plane of rutile TiO_2. There is no crystallographic difference between the samples T1 and T2. Moreover, the HRTEM image of T2 (Fig. 2e) shows that the cuboid crystal facet of nanorod is parallel to the facet {110} and the pyramid-shaped facet is parallel to the facet {111}. The TiO_2 crystal preferably grew along the [001] direction to form nanorods in micron-length but nano-sized diameter due to the lowest formation energy of {110} facet [11]. Fig. 2c and f show the TEM images of T1-Ni and T2-Ni after $Ni(OH)_2$ decoration on the as-prepared TiO_2. As can be seen from Fig. 2c (highlighted by red circle), $Ni(OH)_2$ nanosheet clusters accumulate and locate between the TiO_2 rods of T1-Ni, possibly attributed to the available big gaps between the loosely packing nanorods. Different from the sample T1-Ni, T2-Ni consists of relatively densely agglomerated TiO_2 nanorods, thus the small gaps among the nanorods might promote the $Ni(OH)_2$ nanosheet clusters to evenly distribute and deposit on the TiO_2 surfaces (highlighted by red circle in Fig. 2f). Interestingly, some dot-like $Ni(OH)_2$ particles with sizes of ~5 nm are also found attached to the surfaces of TiO_2 nanorod aggregates, which are not observed in the TEM image of T1-Ni (Fig. 2c). We believe that they might be formed by excessive Ni source after the coverage of $Ni(OH)_2$ clusters inside the small pores and on the external surfaces of T2 during modification.

Fig. 3 shows the XRD patterns of T1, T2, T1-Ni, and T2-Ni, in comparison to P25, which is composed of mainly anatase and some rutile phase. The XRD patterns of T1 and T2 both present characteristic reflections of rutile TiO_2 according to JCPDF#21-1276; whilst the sharp diffraction peaks suggest the high crystallinity of the samples. The crystallite sizes of T1 and T2, calculated using Scherrer equation based on the (110) reflections, are 6 nm and 7 nm, respectively. The crystallite size of P25 was calculated to be 16.5 nm using Scherrer equation based on the (101) anatase peak, which is twice the size of T1 and T2. In addition, the XRD patterns of T1-Ni and T2-Ni show very clear and sharp diffraction peaks at $2\theta = 38.54^\circ$, corresponding to the (101) plane of $Ni(OH)_2$ (JCPDF#14-0117). This indicates the presence of $Ni(OH)_2$ in both samples. Furthermore, the crystallite sizes calculated based on the (110) diffraction peaks of T1-Ni and T2-Ni are as the same as those of T1 and T2. This confirms the deposition of $Ni(OH)_2$ onto T1 and T2 does not change the crystallite sizes of TiO_2. It might be explained by that the $Ni(OH)_2$ deposition took place after the completion of TiO_2 crystallization and such ambient temperature deposition did not have sufficient energy to further promote crystal growth [24].

Fig. 4a presents the UV–vis diffuse reflectance spectra of T1, T2, T1-Ni, and T1-N2 as compared with P25. The bandgap energy values

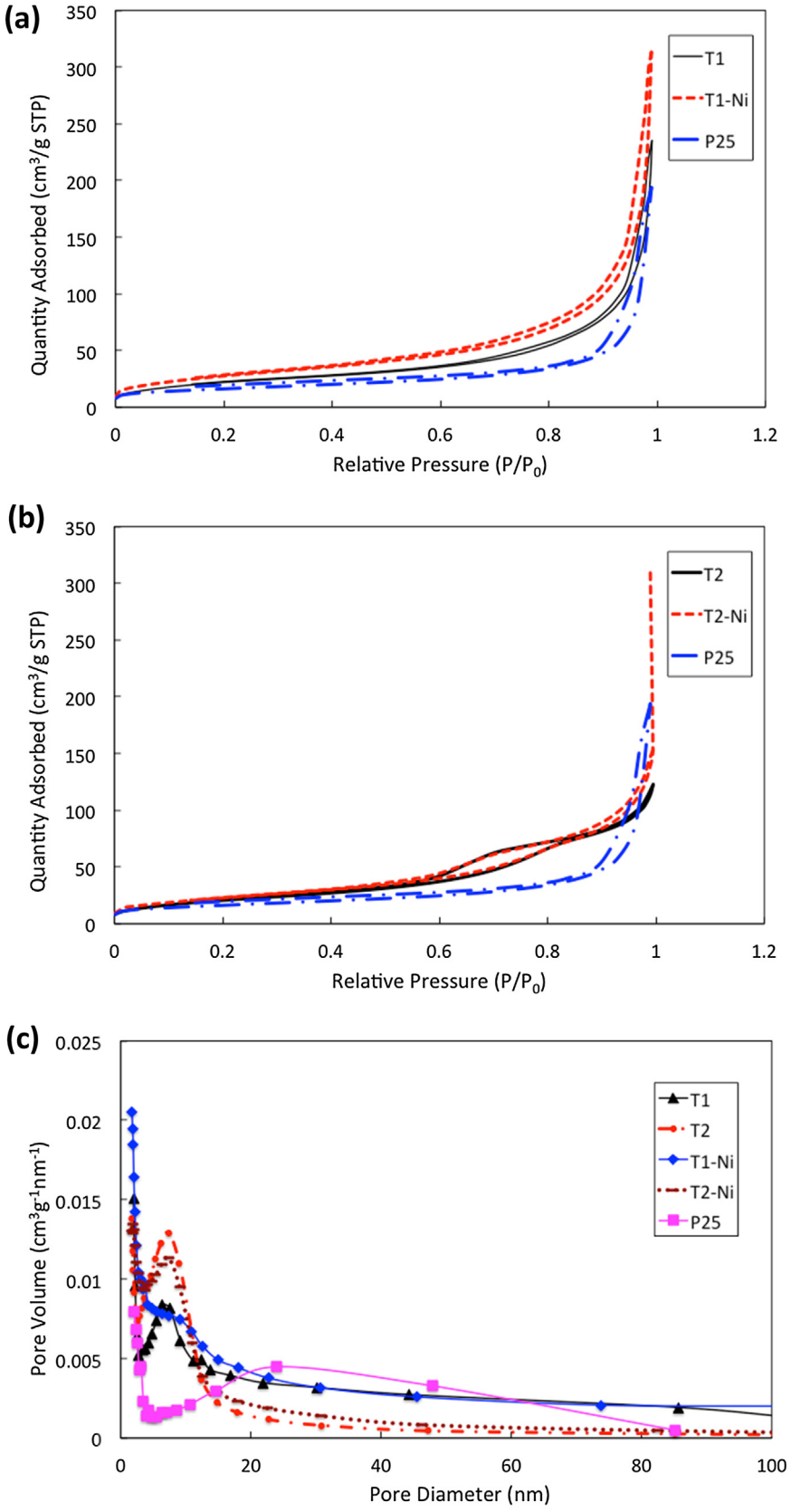

Fig. 5. Nitrogen adsorption-desorption isotherms (a and b) and pore size distribution curves (c) of T1, T2, T1-Ni, T2-Ni and P25.

of samples, calculated from the UV–vis diffuse reflectance spectra shown in Fig. 4b. The T1 and T2 samples, which are comprised of pure rutile TiO_2, show band-edge absorption at 410 nm, corresponding to the bandgap energy of 3.01 ± 0.005 eV. They are lower than 3.20 ± 0.005 eV, the bandgap energy of the commercial TiO_2, P25. After the deposition of $Ni(OH)_2$ onto TiO_2, the spectra show

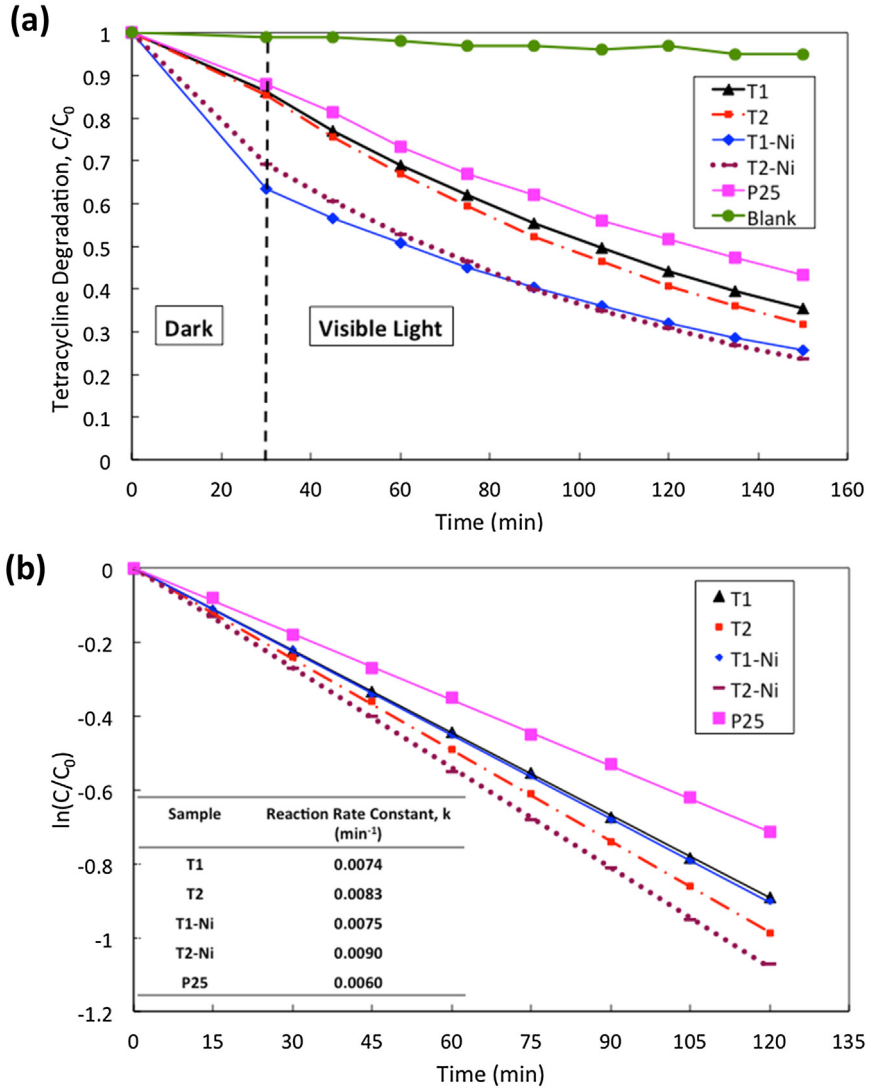

Fig. 6. (a) Tetracycline removal *via* adsorption in the dark and photodegradation under visible light using T1, T2, T1-Ni, T2-Ni and P25 (Blank: photolysis without adding catalyst); (b) kinetic plots for photodegradation of tetracycline (Inset: reaction rate constants).

additional absorption in the region from 600 nm to 800 nm, which is not observed in that of either T1 or T2; this is assigned to the Ni(II) d-d transition [24]. As shown in Fig. 4b, the bandgap energy of T1-Ni and T2-Ni is further reduced down to 2.95 ± 0.005 eV; indicating both the samples could be excited under visible light irradiation.

The nitrogen adsorption-desorption isotherms and pore size distribution curves of T1, T2, T1-Ni, and T2-Ni are shown in Fig. 5a–c, as compared to those of P25; Table 1 summarizes the corresponding BET surface areas, pore volumes and average pore sizes. The isotherms shown are type IV from Brunauer–Deming–Deming–Teller (BDDT) classification, suggesting the presence of mesopores [29]. The shapes of hysteresis loops at a high relative pressure range of 0.8–1.0 are of type H3, revealing the existence of slit-like pores [24]. As can be seen in Table 1, T1 and T2 have similar BET surface areas, which is greater than P25. The pore size and pore volume of T1 are almost a two-fold increase compared to those of T2; which might result from its loosely packing of nanorods (Figs. 1 b and 2 a). The decoration of $Ni(OH)_2$ on the T1 or T2 sample not only lowers the bandgap energy (Fig. 4b), but also increases the BET surface area, pore volume and average pore size (Table 1). This is because of small-size $Ni(OH)_2$ clusters deposited. All the samples (T1, T2, T1-Ni, and T2-Ni) synthesized in this work exhibit higher BET surface areas and smaller bandgap energies in comparison to P25; which are expected to exhibit superior photocatalytic performances and thus work as efficient catalysts.

Fig. 6a shows an overview on the tetracycline removal when using the as-prepared samples *via* adsorption in the dark (30 min) and subsequent photodegradation under visible light (2 h). P25 was also tested under the same condition for comparison. The tetracycline degradation kinetic study is shown in Fig. 6b with the reaction rate constants tabulated as an inset.

After 30 min in the dark, the tetracycline removal using P25 is 12%, which is slightly (approximately 2%) lower than that of T1 and T2 (Fig. 6a). This can be explained by the higher BET surface areas of T1 and T2, which have more active absorption sites. After the adsorption process in the dark, visible light irradiation was introduced, initiating the photocatalytic degradation of tetracycline. It is noted that only a slight variation in tetracycline concentration was observed in the absence of photocatalyst when the solution was exposed to simulated sunlight for 2 h (Blank in Fig. 6a); this strongly confirms that the photolysis of tetracycline is minor even though tetracycline is categorized as one of the photo-sensitized antibiotics [30]. Degradation of tetracycline under visible light without any photocatalyst is slow and dependence of the presence of natural components such as nitrate and humic acids [31]. As can be seen in Fig. 6a and b, both T1 and T2 exhibit significant photo-

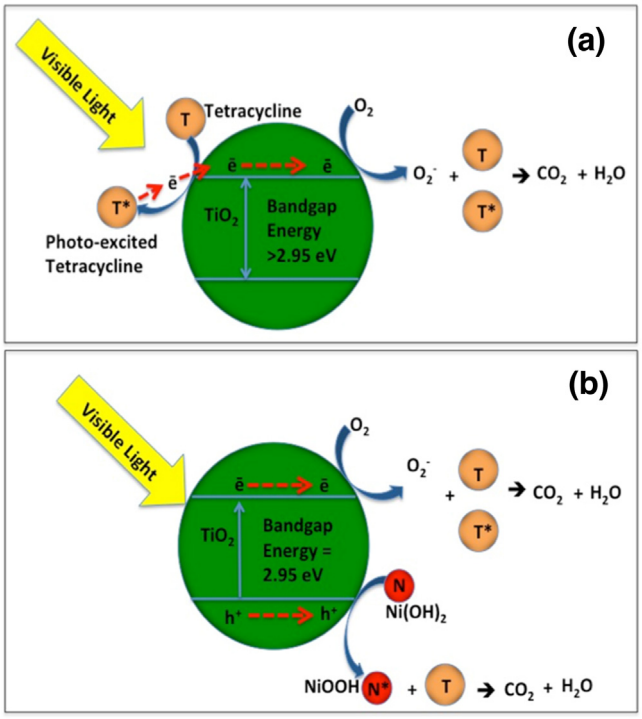

Fig. 7. Proposed photocatalytic oxidation mechanism for samples T-1, T-2, P25 (a), and T1-Ni and T2-Ni (b).

catalytic activities, leading to total tetracycline removal rates of 65% and 68%, respectively; by contrast, only 57% removal was achieved by P25. This can be explained by the fact that the narrower bandgap energies of T1 and T2 result in more super oxide radicals under solar light, and the higher BET surface area also leads to enhanced tetracycline adsorption onto the TiO_2 surface, facilitating photodegradation.

The bandgap energy of T1, T2 and P25 shows that a shorter light wavelength with <420 nm is needed to excite the electrons ($\bar{e}$) from the valance band to generate photoexcited holes (h^+). Thus, the electrons in P25, T1 and T2 cannot be excited to the conduction band, and due to this reason the holes are not effectively generated under visible light. Note that the hydroxyl radicals are not generated here because they can be only produced during the process of water oxidation by photoexcited holes. However, the adsorbed tetracycline on TiO_2 helps to absorb visible light, like the sensitized dye in solar cell, and then excite the electrons and injected into the conduction band of TiO_2. In turn, tetracycline is excited and labeled as T^* and demonstrated in Fig. 7a. The electrons on the conduction band would react with molecule oxygen in the water and generate super oxide radicals, O_2^-. P25, composed of mostly anatase phase and a small amount of rutile phase, produced less O_2^- compared to T1 and T2 that are pure rutile phase [10]. It is an active oxygen species that plays the role in oxidizing tetracycline into CO_2 and H_2O. On the other hand, higher specific surface area of T1 or T2 (more reactive sites) is another factor in promoting photocatalytic process. Moreover, the nanorod-aggregated architectures of T1 and T2 may offer advantageous features to enhance visible light scattering and absorption property as well as reduce recombination rate of photogenerated electrons and holes [26–28]. Especially, the sample T2 with the largest surface area performs best in terms of adsorption and photodegradation, as compared with T1 and P25.

After deposition of $Ni(OH)_2$ onto T1 and T2, the adsorption capacity of the resulting T1-Ni and T2-Ni are greatly improved (Fig. 6a). Undoubtedly, as compared with those of T1 or T2, the approximately two-fold increase of adsorption (37% and 31%) for respective T1-Ni and T2-Ni can be attributed to the deposition of $Ni(OH)_2$ clusters as well as its induced higher specific surface area. The greater specific surface area and lower bandgap energy also lead to the enhanced performances of T1-Ni and T2-Ni in the photocatalytic degradation of tetracycline. After 30 min in dark and subsequently 2 h exposure to visible light, 74% and 76% removal rates are achieved by using T1-Ni and T2-Ni (Fig. 6a). The higher removal rates of tetracycline by T1-Ni and T2-Ni after 150 min process can be attributed to enhanced adsorption ability by $Ni(OH)_2$. Fig. 6b shows that the pseudo-first-order reaction rate constants of T1-Ni and T2-Ni are both higher than those of their parent TiO_2. Note that although T2-Ni possesses a lower surface area as compared to T1-Ni, it performs much better in terms of tetracycline photodegradation. In particular, the reaction rate constant of T2-Ni is 0.0090 min^{-1} (inset of Fig. 6b), making it superior to all other samples including P25. This suggests that the coral-like rutile TiO_2 catalyst modified by $Ni(OH)_2$ can harvest and convert solar energy more efficiently to generate superoxide radicals, and subsequently effectively degrade tetracycline in water.

Although the bandgap energy of sample T1-Ni is smaller (2.95 eV), the reaction rate constant for T1-Ni is not improved as much as T2-Ni. This is probably due to the agglomeration of $Ni(OH)_2$ cluster in between the TiO_2 nanorods in T1-Ni. Unlike T2-Ni, the $Ni(OH)_2$ particles are uniformly deposited on the TiO_2 nanorods. Fig. 7 illustrates the proposed photocatalytic oxidation reaction mechanisms for the samples with or without $Ni(OH)_2$ decoration. Due to its narrower bandgap energy in the decorated samples such as T2-Ni, the valence band electrons of TiO_2 can be excited to the conduction band when exposed to visible light (Eq. (3)). As a result, the photoexcited holes (h^+) are generated on the valence band of TiO_2, which then oxidizes $Ni(OH)_2$ on the TiO_2 nanorods to NiOOH [32,33] (Eq. (4)). NiOOH is a very active catalyst for the reaction of oxidation of organic pollutants [33,34] and it is believed that NiOOH plays an important role in oxidizing the tetracycline in this system. Furthermore, the introduction of $Ni(OH)_2$ onto TiO_2 can effectively inhibit the rapid recombination between conduction band electrons and valence band holes, allowing the generation of highly reactive O_2^- from molecular oxygen, which enhance the process of photocatalytic degradation of tetracycline.

$$TiO_2 + h\nu \rightarrow TiO_2^* + \bar{e} + h^+ \quad (3)$$

$$Ni(OH)_2 + h^+ + OH^- \rightarrow NiOOH + H_2O \quad (4)$$

As discussed above, sample T1-Ni does not improve the reaction rate as much as T2-Ni, which is presumably related to the location of $Ni(OH)_2$ on TiO_2. As can be seen in Fig. 2c, the $Ni(OH)_2$ particles are agglomerated to form large clusters and are found in between the TiO_2 rods in T1-Ni. However, the small $Ni(OH)_2$ particles are found to deposit uniformly on the TiO_2 rods of T2-Ni due to its smaller gaps in between the nanorods (Fig. 2f). The deposition of $Ni(OH)_2$ particles on TiO_2 nanorods, but not in the gaps of the nanorods, could receive the photoexcited holes from TiO_2 and turn into NiOOH to oxidize the tetracycline.

To further investigate the non-photocatalytic effect of $Ni(OH)_2$ decoration, the adsorption experiments were carried out by adding 0.2 g of the as-synthesized samples in 20 mL of 100 ppm tetracycline solution in the dark for 150 min, in comparison with P25 and $Ni(OH)_2$. The results are presented in Fig. 8. $Ni(OH)_2$ is an excellent adsorbent, fully removing tetracycline from the water within 150 min. T1-Ni and T2-Ni show similar adsorption capacity, adsorbing 65.2% and 66.6% of tetracycline, respectively; whereas T1 and T2 only adsorb 50.3% and 53.6%, respectively. By contrast, 45.9% of tetracycline is removed by P25. These results confirm that the enhanced adsorption capacity is another important factor in contributing to improved tetracycline removal efficiency by decorating $Ni(OH)_2$ onto TiO_2 mesocrystals.

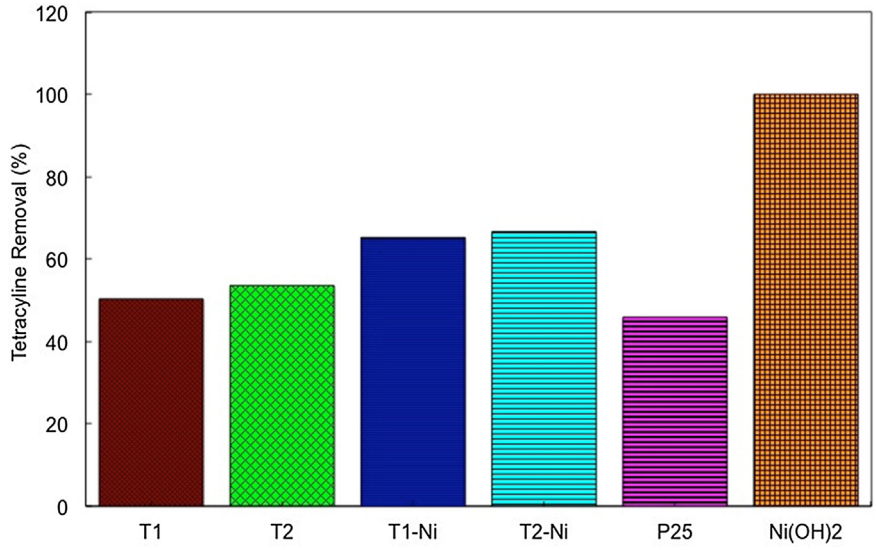

Fig. 8. Tetracycline removal *via* adsorption in the dark using T1, T2, T1-Ni, T2-Ni, P25, and $Ni(OH)_2$ for 150 min.

4. Conclusions

In conclusion, a simple and effective method was developed to synthesize flower-like and coral-like nanorod-aggregated rutile TiO_2 (T1 and T2). Thanks to large surface area, small average pore size and reduced bandgap energy, both rutile TiO_2 catalysts exhibited improved properties in terms of adsorption and photocatalytic degradation of tetracycline under visible light. The modification of the as-prepared rutile TiO_2 mesocrystals with $Ni(OH)_2$ resulted in further enhancement in the removal of tetracycline from water. The visible light-driven photocatalytic degradation demonstrated in this work provides an attractive option to effectively treat secondary effluent which contains tetracycline from conventional water treatment plants in a short reaction period. Its relatively easy operation also provides great potential for integration into currently existing water treatment systems, which would eventually lower the energy consumption and cost in water treatment processes.

Acknowledgements

This work was supported by the Australian Research Council. H.W. thanks the Australian Research Council for a Future Fellowship (Project no. FT100100192). The authors acknowledge use of the facilities at the Monash Centre for Electron Microscopy.

References

[1] I. Chopra, M. Roberts, Tetracycline antibiotics: mode of action, applications, molecular biology, and epidemiology of bacterial resistance, Microbiol. Mol. Biol. Rev. 65 (2001) 232–260.
[2] I. de Godos, R. Muñoz, B. Guieysse, Tetracycline removal during wastewater treatment in high-rate algal ponds, J. Hazard. Mater. 229–230 (2012) 446–449.
[3] H. Kim, Y. Hong, J.-e. Park, V.K. Sharma, S.-i. Cho, Sulfonamides and tetracyclines in livestock wastewater, Chemosphere 91 (2013) 888–894.
[4] M. Liu, Y. Zhang, M. Yang, Z. Tian, L. Ren, S. Zhang, Abundance and distribution of tetracycline resistance genes and mobile elements in an oxytetracycline production wastewater treatment system, Environ. Sci. Technol. 46 (2012) 7551–7557.
[5] I.S. Cho, Z. Chen, A.J. Forman, D.R. Kim, P.M. Rao, T.F. Jaramillo, X. Zheng, Branched TiO_2 nanorods for photoelectrochemical hydrogen production, Nano Lett. 11 (2011) 4978–4984.
[6] A.V. Puga, A. Forneli, H. García, A. Corma, Hydrogen production: production of H_2 by ethanol photoreforming on Au/TiO_2, Adv. Funct. Mater. 24 (2014) 240.
[7] V. Vaiano, O. Sacco, D. Sannino, P. Ciambelli, S. Longo, V. Venditto, G. Guerra, N-doped TiO_2/s-PS aerogels for photocatalytic degradation of organic dyes in wastewater under visible light irradiation, J. Chem. Technol. Biotechnol. 89 (2014) 1175–1181.
[8] Z. Jiang, F. Yang, N. Luo, B.T.T. Chu, D. Sun, H. Shi, T. Xiao, P.P. Edwards, Solvothermal synthesis of N-doped TiO_2 nanotubes for visible-light-responsive photocatalysis, Chem. Commun. 0 (2008) 6372–6374.
[9] J. Zhang, P. Zhou, J. Liu, J. Yu, New understanding of the difference of photocatalytic activity among anatase, rutile and brookite TiO_2, Phys. Chem. Chem. Phys. 16 (2014) 20382–20386.
[10] Y. Kakuma, A.Y. Nosaka, Y. Nosaka, Difference in TiO_2 photocatalytic mechanism between rutile and anatase studied by the detection of active oxygen and surface species in water, Phys. Chem. Chem. Phys. 17 (2015) 18691–18698.
[11] L. Li, J. Yan, T. Wang, Z.-J. Zhao, J. Zhang, J. Gong, N. Guan, Sub-10 nm rutile titanium dioxide nanoparticles for efficient visible-light-driven photocatalytic hydrogen production, Nat. Commun. 6 (2015) 5881.
[12] K.-N.P. Kumar, K. Keizer, A.J. Burggraaf, T. Okubo, H. Nagamoto, S. Morooka, Densification of nanostructured titania assisted by a phase transformation, Nature 358 (1992) 48–51.
[13] F.D. Hardcastle, H. Ishihara, R. Sharma, A.S. Biris, Photoelectroactivity and Raman spectroscopy of anodized titania (TiO_2) photoactive water-splitting catalysts as a function of oxygen-annealing temperature, J. Mater. Chem. 21 (2011) 6337–6345.
[14] S. Yurdakal, G. Palmisano, V. Loddo, O. Alagoz, V. Augugliaro, L. Palmisano, Selective photocatalytic oxidation of 4-substituted aromatic alcohols in water with rutile TiO_2 prepared at room temperature, Green Chem. 11 (2009) 510–516.
[15] K. Ding, Z. Miao, B. Hu, G. An, Z. Sun, B. Han, Z. Liu, Study on the anatase to rutile phase transformation and controlled synthesis of rutile nanocrystals with the assistance of ionic liquid, Langmuir 26 (2010) 10294–10302.
[16] Y. Li, J. Liu, Z. Jia, Morphological control and photodegradation behavior of rutile TiO_2 prepared by a low-temperature process, Mater. Lett. 60 (2006) 1753–1757.
[17] J. Lin, Y.-U. Heo, A. Nattestad, Z. Sun, L. Wang, J.H. Kim, S.X. Dou, 3D hierarchical rutile TiO_2 and metal-free organic sensitizer producing dye-sensitized solar cells 8.6% conversion efficiency, Sci. Rep. 4 (2014) 5769.
[18] S. Kirit, S. Dimple, Characterization of nanocrystalline cobalt doped TiO_2 sol–gel material, J. Cryst. Growth 352 (2012) 224–228.
[19] M. Nishikawa, R. Takanami, F. Nakagoshi, H. Suizu, H. Nagai, Y. Nosaka, Dominated factors for high performance of Fe^{3+} grafted metal doped TiO_2 based photocatalysts, Appl. Catal. B 160–161 (2014) 722–729.
[20] D. Chen, Z. Jiang, J. Geng, Q. Wang, D. Yang, Carbon and nitrogen Co-doped TiO_2 with enhanced visible-light photocatalytic activity, Ind. Eng. Chem. Res. 46 (2007) 2741–2746.
[21] H. Irie, Y. Watanabe, K. Hashimoto, Carbon-doped anatase TiO_2 powders as a visible-light sensitive photocatalyst, Chem. Lett. 32 (2003) 772–773.
[22] F. Dong, W. Zhao, Z. Wu, Characterization and photocatalytic activities of C, N and S co-doped TiO_2 with 1D nanostructure prepared by the nano-confinement effect, Nanotechnology 19 (2008) 365607.
[23] X. Cai, Y. Cai, Y. Liu, S. Deng, Y. Wang, Y. Wang, I. Djerdj, Photocatalytic degradation properties of $Ni(OH)_2$ nanosheets/ZnO nanorods composites for azo dyes under visible-light irradiation, Ceram. Int. 40 (2014) 57–65.
[24] J. Yu, Y. Hai, B. Cheng, Enhanced photocatalytic H_2-Production activity of TiO_2 by $Ni(OH)_2$ cluster modification, J. Phys. Chem. C 115 (2011) 4953–4958.
[25] J. Liao, S. Lin, N. Pan, S. Li, X. Cao, Y. Cao, Fabrication and photocatalytic properties of free-standing TiO_2 nanotube membranes with through-hole morphology, Mater. Charact. 66 (2012) 24–29.

[26] H. Wang, Y. Bai, Q. Wu, W. Zhou, H. Zhang, J. Li, L. Guo, Rutile TiO_2 nano-branched arrays on FTO for dye-sensitized solar cells, Phys. Chem. Chem. Phys. 13 (2011) 7008–7013.
[27] Y. Li, M. Guo, M. Zhang, X. Wang, Hydrothermal synthesis and characterization of TiO_2 nanorod arrays on glass substrates, Mater. Res. Bull. 44 (2009) 1232–1237.
[28] S. Liang, F. Teng, G. Bulgan, R. Zong, Y. Zhu, Effect of phase structure of MnO_2 nanorod catalyst on the activity for CO oxidation, J. Phys. Chem. C 112 (2008) 5307–5315.
[29] K.S.W. Sing, D.H. Everett, R.A.W. Haul, L. Moscou, R.A. Pierotti, J. Rouquerol, T. Siemieniewska, Reporting physisorption data for gas/solid systems with special reference to the determination of surface area and porosity, Pure Appl. Chem. 57 (1985) 603–619.
[30] A.A. Borghi, M.S.A. Palma, Tetracycline: production, waste treatment and environmental impact assessment, Braz. J. Pharm. Sci. 50 (2014) 25–40.
[31] R. Andreozzi, M. Raffaele, P. Nicklas, Pharmaceuticals in STP effluents and their solar photodegradation in aquatic environment, Chemosphere 50 (2003) 1319–1330.
[32] G. Wang, Y. Ling, X. Lu, H. Wang, F. Qian, Y. Tong, Y. Li, Solar driven hydrogen releasing from urea and human urine, Energy Environ. Sci. 5 (2012) 8215–8219.
[33] S. Xie, T. Zhai, W. Li, M. Yu, C. Liang, J. Gan, X. Lu, Y. Tong, Hydrogen production from solar driven glucose oxidation over $Ni(OH)_2$ functionalized electroreduced-TiO_2 nanowire arrays, Green Chem. 15 (2013) 2434–2440.
[34] B.V. Lyalin, V.A. Petrosyan, Oxidation of organic compounds on NiOOH electrode, Russ. J. Electrochem. 46 (2010) 1199–1214.